Phase diagram of electron-doped dichalcogenides

M. Rösner, S. Haas, and T. O. Wehling

Phys. Rev. B **90**, 245105 — Published 1 December 2014

DOI: 10.1103/PhysRevB.90.245105

Phase Diagram of Electron Doped Dichalcogenides

M. Rösner,[1,2,*] S. Haas,[3] and T. O. Wehling[1,2]

[1] *Institut für Theoretische Physik, Universität Bremen, Otto-Hahn-Allee 1, 28359 Bremen, Germany*
[2] *Bremen Center for Computational Materials Science, Universität Bremen, Am Fallturm 1a, 28359 Bremen, Germany*
[3] *Department of Physics and Astronomy, University of Southern California, Los Angeles, CA 90089-0484, USA*

(Dated: November 10, 2014)

Using first principle calculations, we examine the sequence of phases in electron doped dichalcogenides, such as recently realized in field-gated MoS_2. Upon increasing the electron doping level, we observe a succession of semiconducting, metallic, superconducting and charge density wave regimes, i.e. in different order compared to the phase diagram of metallic dichalcogenides such as $TiSe_2$. Both instabilities trace back to a softening of phonons which couple the electron populated conduction band minima. The superconducting dome, calculated using Eliashberg theory, is found to fit the experimentally observed phase diagram, obtained from resistivity measurements. The charge density wave phase at higher electron doping concentrations as predicted from instabilities in the phonon modes is further corroborated by detecting the accompanying lattice deformation in density functional based supercell relaxations. Upon charge density wave formation, doped MoS_2 remains metallic but undergoes a Lifschitz transition, where the number of Fermi pockets is reduced.

I. INTRODUCTION

Several materials including graphene or transition metal dichalcogenides can be prepared at monolayer thickness.[1] Because of their low effective dimensionality, there is a lack of screening in these materials, and in addition the band structure shows strong van Hove singularities. This can lead to strong enhancements of scales and result in competing instabilities, such as superconductivity (SC) and charge density wave (CDW) phases.[2,3] For example, based on Eliashberg theory it has been argued that by doping the structurally related graphene up to its van Hove singularity, the effective electron-phonon coupling can be greatly enhanced, leading to superconducting transition temperatures potentially as high as 30K.[4] Thereby, the quasi-two-dimensional structure of these compounds allows for a high degree of control via tuning knobs such as pressure, strain, doping and adsorbates, but it also makes these materials more vulnerable to the effects of impurity disorder.

The generic phase diagram of the metallic transition metal dichalcogenides features a CDW regime at and close to half-filling, which upon *hole doping* or exerting external pressure is suppressed by a competing SC instability.[5,6] For example, pristine 1T-$TiSe_2$ undergoes a CDW phase transition at approximately 200K.[7] Upon hole doping via Cu intercalation[8] or application of pressure[9] this phase is suppressed and replaced by competing SC order with transition temperatures $\sim$ 2-5K, leading to a phase diagram topology akin to the high-T_c cuprates, with CDW taking the place of the antiferromagnetic insulator regime in the cuprates. This succession of phases can be modeled by combining first principle calculations with Eliashberg theory, based on a phonon mediated pairing mechanism.[10] Furthermore, since these materials are quasi-two-dimensional, it can be expected that other low-energy modes, such as plasmons, are present and may contribute to the formation of the SC condensate.[6,11]

In this paper, we focus on the phase diagram of *electron doped* dichalcogenides. Since these materials do not show an electron/hole symmetry it is a priori not known which phases will arise and how they compete with each other. Indeed, we find a different topology in the electron doped regime, thus leading to an interesting set of predictions that can be experimentally tested. Without loss of generality, we focus on the much studied compound MoS_2 because there already is a wealth of data available which allows to scrutinize our approach. Bulk MoS_2 is a layered transition-metal dichalcogenide with an indirect band gap, whereas monolayer MoS_2 is a direct band gap semiconductor.[12,13] Its conduction and valence bands are dominated by the d-orbitals of the Mo atoms.[14] Electron doping of thin-flake MoS_2 has recently been achieved by means of combined liquid/solid high-capacitance gates, leading to effective 2D carrier densities of up to $n_{2D} \approx 1.5 \times 10^{14}$ cm^{-2}. Such doping by field effect gates allows us to access larger carrier concentrations compared to chemical substitution, without substantially deforming the lattice.[15] A field-doping-induced superconducting dome was found with onset at $n_{2D} = 6.8 \times 10^{13}$ cm^{-2} and peak with maximum $T_c = 10.8$ K at $n_{2D} = 1.2 \times 10^{14}$ cm^{-2}.[15,16] Using density functional theory calculations, it has been shown that this superconducting dome is consistent with electron-phonon coupling that is doping-dependent due to the change of Fermi surface topology when negative charge carriers are introduced.[17] Here, we push this analysis further and deliver a quantitative description of the superconducting dome and identify a competing CDW phase which occurs at higher doping concentrations. Although this kind of competition is known in the hole doped regime, it is interesting that the CDW phase exists in the electron doped regime as well. In this case the Fermi surface topology is totally different and thus the behavior of the newly found CDW phase is differ-

ent from the corresponding phase in the hole doped case: Electron doped MoS_2 remains metallic after CDW formation. While it may turn out to be difficult to achieve such high doping concentrations in MoS_2 experimentally by back gating,[15] this prediction is a generic feature, and thus should hold for other electron doped dichalcogenides as well. Example systems for observing the CDW phase predicted here include chemically doped MoS_2, as e.g. realized by alkali deposition/intercalation.[18]

II. METHODS

We use the VASP[19,20] and Quantum Espresso[21] Packages for the density functional theory (DFT) based self-consistent evaluation of the electronic and phononic band structures. Electron doping x (in electrons per primitive MoS_2 unit cell) or $n_{2D} = x/A$ (in electrons per cm^2, A is the area of the unit cell) is realized by introducing additional electrons along with a compensating jellium background. Care is taken such that no unphysical low energy states are introduced by the positive background charges. The electron-phonon coupling matrix elements are calculated using the Phonon package of Quantum Espresso[35], and the superconducting properties based on Eliashberg theory are obtained via postprocessing.[22,23] In particular, the Eliashberg spectral function,

$$\alpha^2F(\omega) = \frac{1}{2\pi N(\epsilon_F)} \sum_{\mathbf{q}\nu} \delta(\omega - \omega_{\mathbf{q}\nu}) \frac{\gamma_{\mathbf{q}\nu}}{\hbar\omega_{\mathbf{q}\nu}}, \qquad (1)$$

is evaluated from the electronic density of states at the Fermi level $N(\epsilon_F)$, the phonon frequencies $\omega_{\mathbf{q}\nu}$ and the line widths $\gamma_{\mathbf{q}\nu}$ which contain the electron-phonon coupling matrix elements.[23] The superconducting transition temperatures can then be estimated using the Allen-Dynes formula,[22]

$$T_c = \frac{\hbar\omega_{log}}{1.2} \exp\left[\frac{-1.04(1+\lambda)}{\lambda(1-0.62\mu^*)-\mu^*}\right], \qquad (2)$$

where

$$\lambda = 2\int d\omega \, \frac{\alpha^2F(\omega)}{\omega} \qquad (3)$$

is the averaged electron-phonon coupling constant,

$$\omega_{log} = \exp\left[\frac{2}{\lambda}\int d\omega \, \alpha^2F(\omega)\frac{\log(\omega)}{\omega}\right] \qquad (4)$$

is the logarithmic averaged typical phonon frequency and μ^* is the effective Coulomb pseudopotential. The newly found emerging CDW at higher electron concentrations is identified by (i) the occurrence of an unstable phonon mode, (ii) by spontaneous deformation of the honeycomb lattice, as well as (iii) by comparison of energies of the deformed lattice with the unperturbed lattice[36]. For these calculations two different unit cells are used. To calculate the phonon dispersion as well as the corresponding electron-phonon coupling matrix elements used in the Eliashberg formalism we use a primitive 1×1 unit cell of MoS_2. Since these calculations will predict an unstable phonon mode at Brillouin zone M points (see results below), we perform relaxations of a 2×1 supercell, which is commensurate with the resulting CDW and which can host the corresponding lattice deformations. The CDW formation energy discussed below is defined by

$$\triangle E_{\mathrm{CDW}} = \frac{E_{2\times1} - E^{\mathrm{CDW}}_{2\times1}}{2}, \qquad (5)$$

where $E_{2\times1}$ is the total energy of the relaxed 2×1 unit cell preserving the 1×1 symmetries (i.e. just doubling of a 1×1 primitive cell with relaxed S atoms) and $E^{\mathrm{CDW}}_{2\times1}$ is the corresponding energy of the fully relaxed 2×1 unit cell which is able to incorporate the CDW.

III. RESULTS

Similar to other dichalcogenides, the low-energy properties in MoS_2 are dominated by minima in the conduction band at Brillouin zone points K and Σ, which have predominantly Mo d_{z^2}-orbital character (at K) as well as Mo d_{xy}- and $d_{x^2-y^2}$-character (at Σ).[12] Upon electron doping, the Σ valley moves towards lower energies, whereas the K valley is less affected (see inset of Fig. 1).[17] The doping levels shown here correspond to the metallic regime, the SC phase, and the CDW phase. These instabilities are discussed in more detail below.

A. Metallic and Superconducting Phase

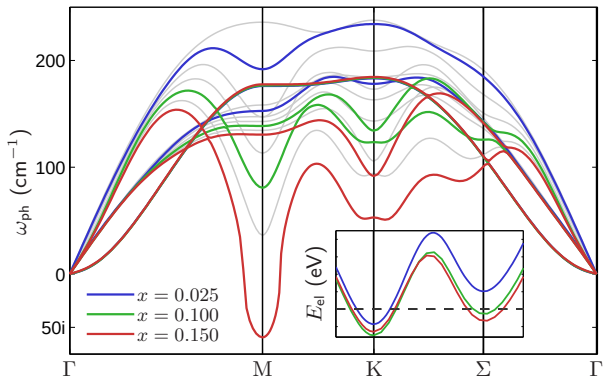

Figure 1: (Color online) Acoustic part of the phononic band structure of MoS_2 for electron doping concentrations $x = 0.025$ (blue), $x = 0.100$ (green), and $x = 0.150$ (red), corresponding to the metallic, superconducting and charge density wave regimes respectively. The inset shows the conduction bands of the corresponding electronic band structures (Fermi levels are indicated by dashed lines, ticks are separated by 100 meV). The phononic band structures are completed by several doping levels in between the range of $x = 0$ to $x = 0.15$ (grey).

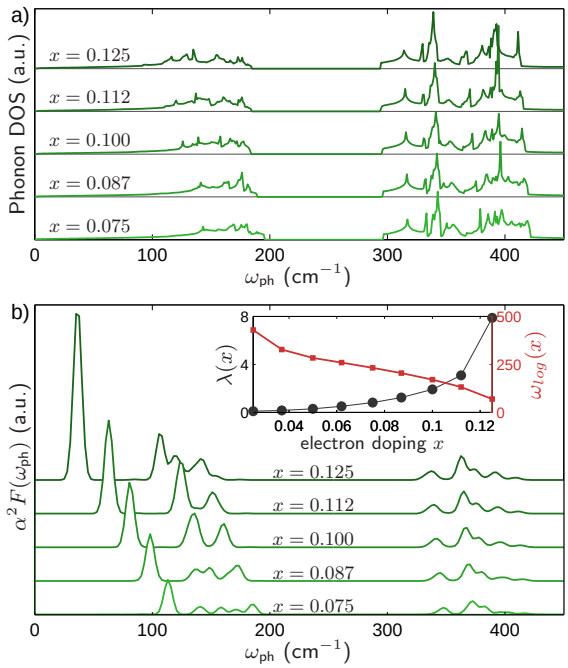

Figure 2: (Color online) (a) Phonon density of states and (b) Eliashberg function of MoS_2 in the SC phase for different doping levels. The inset in (b) shows the evolution of $\lambda(x)$ and $\omega_{log}(x)$ (using a Gaussian smearing of $\delta = 0.005\,\mathrm{Ry}$), determining $T_c(x)$.

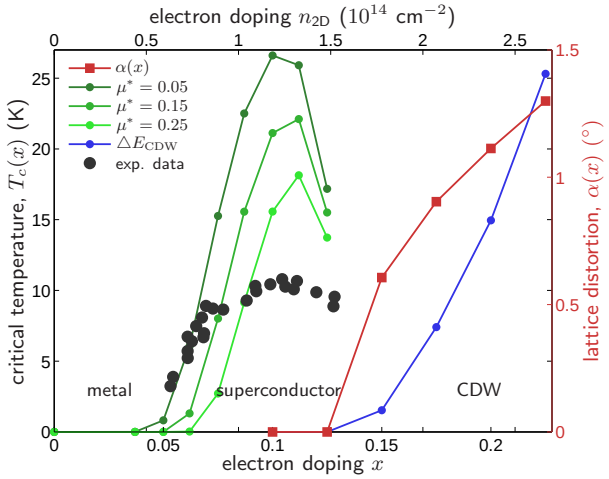

Figure 3: (Color online) Temperature-doping phase diagram of MoS_2. Circles belong to the left axis (K) and squares to the right (°). Green lines are obtained from first principle calculations combined with Eliashberg theory and show the SC critical temperature for different Coulomb pseudopotentials (using a Gaussian smearing of $\delta = 0.005\,\mathrm{Ry}$). Black circles are experimental data.[15] Also shown is the lattice distortion angle α (red squares) and the energy gain upon CDW formation ΔE_{CDW} in K (blue circles) .

The acoustic parts of the phonon dispersions of MoS_2 are shown for the same electron doping concentrations in Fig. 1. Similar to graphene, pristine MoS_2 has one quadratic and two linear acoustic phonon branches which become rather flat at the Brillouin zone boundary (i.e. between K and M) with phonon energies in the range of $\sim 180 - 240\,\mathrm{cm}^{-1}$. Upon doping, the acoustic in-plane branches soften.[24] The parabolic out-of-plane phonons are odd under mirror transformation with respect to the Mo plane and do not couple the conduction band minima at K and Σ. There is thus no Kohn anomaly (or related phenomena) leading to softening of these phonons upon electron doping. As we will see below, the softened regions of the acoustic branches dominate the formation of the SC condensate, with $\omega_{typ} \sim 2\pi k_B T_c$. At a critical electron concentration $x_c \sim 0.14$ one of the acoustic modes develops an instability at the M point, indicating the onset of a CDW regime. At this point the phonon frequency of this mode becomes imaginary (Fig. 1).[10] This behavior is reminiscent of $TiSe_2$, where a CDW-SC transition can be tuned by pressure or Cu intercalation.[9] However, the CDW regime in $TiSe_2$ already occurs in its pristine state, and is suppressed by pressure or hole-doping, giving way to SC, whereas the sequence of phases we observe in MoS_2 is reversed.

Let us now turn our focus toward the SC regime at intermediate doping levels. We examine the lattice dynamics encoded in the phonon density of states and the Eliashberg function. The phonon density of states (Fig. 2 (a)) has a rich peak structure, with the largest contributions stemming from the regions where the phonon dispersion flattens, leading to characteristic van Hove enhancements. While the high-energy optical branches ($\sim 300 - 500\,\mathrm{cm}^{-1}$) lead to the strongest peaks in the phonon density of states, it turns out that they do not contribute significantly to the formation of the SC condensate. The SC response encoded in the Eliashberg function is dominated by the softened acoustic phonon branches around the M and K points. The correspondingly enhanced low energy phonon DOS is inherited by the Eliashberg function (Fig. 2 (b)), which includes weighting by the electron-phonon coupling matrix elements as well as inverse phonon energies.

As the acoustic phonon mode with minimum at the M point softens, the evolution of the Eliashberg function displays a maximum integrated intensity at $x = 0.125$. However, this concentration does not correspond to maximum of $T_c(x)$ since the interplay of the effective coupling $\lambda(x)$ and $\omega_{log}(x)$ has to be considered. As it can be seen in the inset of Fig. 2 (b) $\omega_{log}(x)$ decreases while $\lambda(x)$ increases with increasing doping. An optimal proportion is reached at $x \approx 0.11$ leading to a maximum of T_c.

Thus, the combined evolution of $\lambda(x)$ and $\omega_{log}(x)$ is one reason for the dome-shaped dependence of the SC transition temperature on the electron doping concentration, which can be seen in Fig. 3. Here we show experimental data of Ref. 15 along with results of our numerical simulation for different Coulomb pseudopotentials μ^*. Besides the coincidence in the position of the maximum in $T_c(x)$ at $x \approx 0.11$ ($n_{2D} = 1.2 \times 10^{14}$ cm^{-2}), we also note that the computed and experimental SC transition

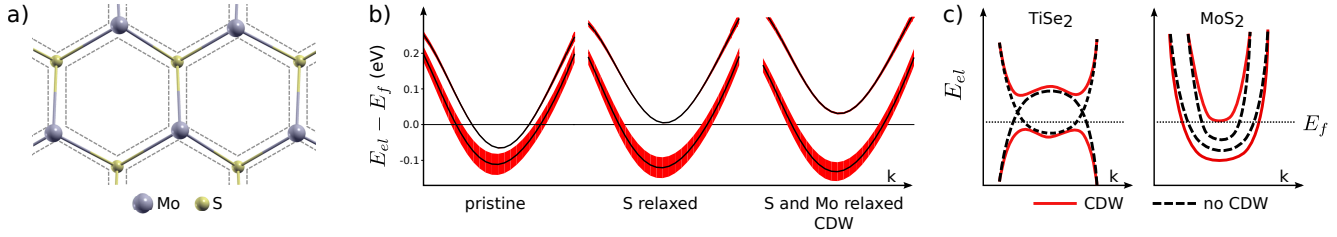

Figure 4: (Color online) Manifestation of the CDW in lattice distortion and band structure. (a) Lattice distortion in MoS_2, observed in ab initio calculations via self-consistent relaxation of 2×1 supercells. (b) Influence of lattice relaxation effects on the band structures of the 2×1 supercells obtained for a doping level $x = 0.2$. The $d_{xy}, d_{x^2-y^2}$ weight of the bands is illustrated by the (red) width of the bands. The middle panel shows the effect of homogeneous outward relaxation of the S atoms on the conduction band minima as observable from comparison of the MoS_2 structure with S positions according to undoped (pristine) and homogeneously relaxed $x = 0.2$ system. The right panel shows the comparison of supercell band structures for homogeneously relaxed MoS_2 and MoS_2 featuring the CDW (fully relaxed) at $x = 0.2$. (c) Comparison of band topologies involved in the CDW formation in $TiSe_2$ and MoS_2. Only in the $TiSe_2$ case, CDW formation can fully gap the Fermi surface.

temperatures are of the same order of magnitude. This is remarkable, since Eliashberg theory is a rather crude approximation, which does not account for pair-breaking effects, such as impurities, incorporates Coulomb interactions only statically as μ^* and neglects enhanced phase fluctuations in 2D. It is therefore expected to overestimate $T_c(x)$.

Beside λ and ω_{log}, the effective Coulomb potential μ^* could be doping dependent as well, since the Fermi surface will change in size and shape upon electron doping. To estimate how such a doping dependent $\mu^*(x)$ would affect the superconducting dome, we calculated T_c in for three different Coulomb pseudopotentials $\mu^* = 0.05$, 0.15, and 0.25. This range is approximately centered around $\mu^* = 0.13$, which has been suggested in Refs. 17,25. The overall trend of an increasing μ^* is obviously a decreasing T_c since the Coulomb repulsion suppresses the electron pairing. In more detail, we find a stronger dependence of T_c to μ^* in the intermediate doping regime $0.05 < x < 0.75$ than for high doping levels. Thereby we see, that for small doping levels a rather small μ^* fits the T_c dome quite well, whereas in the high doping regime a higher value of μ^* describes the dome appropriate.

B. Charge Density Wave Phase

The occurrence of SC and CDW phases in TMDCs is well known.[26–29] There are several examples in which a phase transition between these two states appears or where CDW and SC phases coexist.[26–29] A promient (and controversially debated[30,31]) example in this sense is the CDW/SC phase transition under pressure in 1T-$TiSe_2$.[10] 1T-$TiSe_2$ and electron doped MoS_2 have in common, that their Fermi surface consists of multiple pockets with different orbital characters. Additionally both systems share strong electron-phonon coupling, which leads to the CDW phase and manifests as an unstable acoustic phonon mode at M in both systems. Nevertheless, there are crucial differences between these two systems: In Refs. 10,30,31 the bulk system has been studied, whereas here the monolayer system is under consideration. Furthermore the Fermi surface topologies differ in the number of electron/hole pockets (c.f. Fig. 4 c). In bulk 1T-$TiSe_2$ the Fermi surface consists of electron and hole pockets, while in electron doped monolayer MoS_2 there are electron pockets only. Additionally, orbital characters near the Fermi level alter between the two materials. Finally, in monolayer MoS_2 there are also phonon modes at K and in the vicinity of Σ, which soften upon charge doping, in contrast to 1T-$TiSe_2$.

In order to better understand the nature of the SC-CDW phase transition in MoS_2, we examine the doping dependence of the M point CDW-induced lattice distortion α in a 2×1 supercell, shown as a red line in Fig. 3. Here, α is defined as the angle between three neighboring Mo atoms subtracted by 60°. For an undistorted honeycomb lattice one finds $\alpha = 0$. By relaxing the atomic structure of the supercell, we observe $\alpha \neq 0$ beyond a critical electron concentration of $x_c \approx 0.14$, as forces arise due to the unstable M-point phonon mode. These distortion effects, depicted in Fig. 4 (a), become more pronounced with increasing electron doping. We note that in addition to the CDW formation, there is a further homogeneous outward relaxation of the S atoms upon electron doping.

The effects of homogeneous S relaxation and CDW formation on the electronic structure are illustrated in Fig. 4 (b) for electron doping $x = 0.2$.[37] In the supercell Brillouin zone, the former band minima at K and Σ are folded almost on top of each other at the supercell K point. In the absence of a CDW, low-energy states originating from K and Σ can be distinguished by their orbital band character. The latter states carry a significant $d_{xy}/d_{x^2-y^2}$-weight, whereas the conduction band minimum at K has no such admixture (see Fig. 4 (b) left panel). The outward relaxation of the S atoms lowers $d_{xy}/d_{x^2-y^2}$-derived states from Σ in energy (Fig. 4 (b) middle panel). With increasing CDW amplitude the

two bands originating from K and Σ mix, and this hybridization adds to the splitting of the two bands, c.f. Fig. 4 (b) (right panel). This splitting leads to lowering of the electronic energy if the Fermi level lies sufficiently high in the conduction band. The total energy gain upon CDW formation as function of doping level ($\triangle E_{\mathrm{CDW}}$) is shown in Fig. 3 (blue line). It illustrates that the CDW formation energies for $x < 0.25$ are comparable to typical Cooper pair condensation energies $\sim 10\,\mathrm{K}$ ($\sim 1\,\mathrm{meV}$) encountered here, and an interesting competition of the two should emerge.

While the Eliashberg theory of SC order is only applicable as long as the lattice remains stable, it is clear that the competition of CDW and SC order will in any case depend on changes of the Fermi surface due to CDW formation. For the perfect crystal (relaxed structure at zero doping) and a doping level of $x = 0.2$, two bands would intersect the Fermi level near the supercell K point, and there would be thus two Fermi lines around K. Upon outward relaxation of the S atoms (preserving all lattice symmetries) and formation of the CDW, we observe a Lifschitz transition where one of the Fermi pockets disappears, Fig. 4 (b) (middle and right panel). The system thus remains metallic in the CDW phase, but the SC transition temperatures should be reduced due to the vanishing phase space for inter-pocket scattering. Persisting metallicity in the CDW phase of MoS_2 is indeed ensured by the "topology" of the inter-mixing bands at K and Σ, Fig. 4 (c). In $TiSe_2$, CDW bands with opposite slope are folded on top of each other, and a gap can open upon hybridization. However, in MoS_2, the slopes of the backfolded bands have the same sign, and avoided crossings do not lead to a full gap, but only reduce the number of Fermi sheets by one.

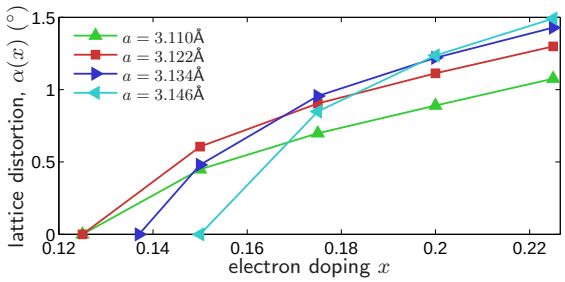

Figure 5: (Color online) Lattice distortion angle α upon CDW formation in dependence of the electron doping for different lattice constants.

Since it is known, that the energies of the minima in the conduction band of MoS_2 are very sensitive to external strain[32] the before mentioned change in the Fermi surface topology due to the CDW transition might be sensitive to strain as well. To analyze this behavior we performed supercell relaxation calculations for different lattice constants and show corresponding lattice distortions upon CDW formation in dependence of the electron doping in Fig. 5. The red curve ($a = 3.122\,\text{Å}$) is the same as in Fig. 3. Here we provide the corresponding data for a smaller ($a = 3.110\,\text{Å}$) as well as for two bigger ($a = 3.134\,\text{Å}$ and $a = 3.146\,\text{Å}$) lattice constants. The differences between these values are less than 1%. However, as it can be seen in Fig. 5 the critical concentration for the onset of the CDW changes from $x_c \approx 0.14$ to $x_c \approx 0.17$ upon increasing the lattice constant. This is a change of more than 17%. The behavior at high doping changes as well and tends to bigger distortion angles with an increasing lattice constant. The competition between the CDW and the SC phases is therefore sensitive to both, the electron doping level and external strain.

IV. CONCLUSIONS

Electron doped dichalcogenides feature CDW and SC instabilities, driven by the softening of an acoustic phonon mode upon charge doping. Due to the band topology, the M point CDW cannot fully gap the Fermi surface of electron doped MoS_2. Therefore, CDW and SC phases may coexist, albeit with reduced SC transition temperatures. In any case, the SC and CDW instabilities rely on the energy differences between the conduction band minima at K and Σ. These are highly sensitive to lattice relaxation, and we speculate that adsorption of molecular species on MoS_2 may be useful for tuning superconducting transition temperatures.

Since MoS_2 is optically active, it remains to be seen whether intense photodoping could be a means to trigger the CDW or SC instabilities. This would be a rather unusual effect, since excitations normally suppress order and have been widely used to melt CDWs.[33,34]

The competition of CDW and SC phases is common in metallic transition metal dichalcogenides, such as $TiSe_2$, $NbSe_2$ and TaS_2. All these materials differ, however, from MoS_2 in that the transition metal atoms lack one (Nb, Ta) or two (Ti) valence electrons in comparison to Mo. Nevertheless, electron doped MoS_2 develops CDW/SC instabilities as well, although entirely different bands are involved. The most prominent resulting difference compared to materials like $TiSe_2$ is the reversed order in the phase diagram of MoS_2.

Acknowledgments: We are grateful for useful discussions with A.V. Balatsky, I. Gierz, A. Liu, F. Mauri, and M. Calandra. S.H. would like to the thank the Humboldt Foundation for support. This work was supported by the European Graphene Flagship and by the Department of Energy under Grant No. DE-FG02-05ER46240. The numerical computations were carried out on the University of Southern California high performance supercomputer cluster and the Norddeutscher Verbund zur Förderung des Hoch- und Höchstleistungsrechnens (HLRN) cluster.

* Electronic address: mroesner@itp.uni-bremen.de

[1] K. S. Novoselov, D. Jiang, F. Schedin, T. J. Booth, V. V. Khotkevich, S. V. Morozov, and A. K. Geim, Proc. Natl. Acad. Sci. USA **102**, 10451 (2005).

[2] K. C. Rahnejat, C. A. Howard, N. E. Shuttleworth, S. R. Schofield, K. Iwaya, C. F. Hirjibehedin, C. Renner, G. Aeppli, and M. Ellerby, Nature Communications **2**, 558 (nov 2011).

[3] Q. H. Wang, K. Kalantar-Zadeh, A. Kis, J. N. Coleman, and M. S. Strano, Nature Nanotechnology **7**, 699 (2012), ISSN 1748-3387.

[4] C. Si, Z. Liu, W. Duan, and F. Liu, Phys. Rev. Lett. **111**, 196802 (Nov 2013).

[5] A. H. Castro Neto, Phys. Rev. Lett. **86**, 4382 (May 2001).

[6] J. van Wezel, P. Nahai-Williamson, and S. S. Saxena, Phys. Rev. B **83**, 024502 (Jan 2011).

[7] F. J. Di Salvo, D. E. Moncton, and J. V. Waszczak, Phys. Rev. B **14**, 4321 (Nov 1976).

[8] E. Morosan, H. Zandbergen, B. Dennis, J. Bos, Y. Onose, T. Klimczuk, A. Ramirez, N. Ong, and R. Cava, Nat Phys **2**, 544 (2006).

[9] A. F. Kusmartseva, B. Sipos, H. Berger, L. Forró, and E. Tutiš, Phys. Rev. Lett. **103**, 236401 (Nov 2009).

[10] M. Calandra and F. Mauri, Phys. Rev. Lett. **106**, 196406 (May 2011).

[11] T. O. Wehling, E. Şaşıoğlu, C. Friedrich, A. I. Lichtenstein, M. I. Katsnelson, and S. Blügel, Phys. Rev. Lett. **106**, 236805 (Jun 2011).

[12] A. Kuc, N. Zibouche, and T. Heine, Phys. Rev. B **83**, 245213 (Jun 2011).

[13] E. S. Kadantsev and P. Hawrylak, Solid State Communications **152**, 909 (2012), ISSN 0038-1098.

[14] G.-B. Liu, W.-Y. Shan, Y. Yao, W. Yao, and D. Xiao, Phys. Rev. B **88**, 085433 (Aug 2013).

[15] J. T. Ye, Y. J. Zhang, R. Akashi, M. S. Bahramy, R. Arita, and Y. Iwasa, Science **338**, 1193 (2012).

[16] K. Taniguchi, A. Matsumoto, H. Shimotani, and H. Takagi, Applied Physics Letters **101**, 042603 (2012).

[17] Y. Ge and A. Y. Liu, Phys. Rev. B **87**, 241408 (Jun 2013).

[18] R. B. Somoano, V. Hadek, A. Rembaum, S. Samson, and J. A. Woollam, The Journal of Chemical Physics **62**, 1068 (1975).

[19] G. Kresse and J. Furthmüller, Comput. Mat. Sci., 15(1996).

[20] G. Kresse and J. Furthmüller, Phys. Rev. B, 11169(1996).

[21] P. Giannozzi, S. Baroni, N. Bonini, M. Calandra, R. Car, C. Cavazzoni, D. Ceresoli, G. L. Chiarotti, M. Cococcioni, I. Dabo, A. Dal Corso, S. de Gironcoli, S. Fabris, G. Fratesi, R. Gebauer, U. Gerstmann, C. Gougoussis, A. Kokalj, M. Lazzeri, L. Martin-Samos, N. Marzari, F. Mauri, R. Mazzarello, S. Paolini, A. Pasquarello, L. Paulatto, C. Sbraccia, S. Scandolo, G. Sclauzero, A. P. Seitsonen, A. Smogunov, P. Umari, and R. M. Wentzcovitch, Journal of Physics: Condensed Matter **21**, 395502 (2009).

[22] P. B. Allen and R. C. Dynes, Phys. Rev. B **12**, 905 (Aug 1975).

[23] G. M. Eliashberg, Zh. Eksp. Teor. Fiz., 966(1960).

[24] Y. Ge, W. Wan, W. Feng, D. Xiao, and Y. Yao arXiv:1403.0695.

[25] W. L. McMillan, Phys. Rev. **167**, 331 (Mar 1968).

[26] R. B. Somoano, V. Hadek, A. Rembaum, S. Samson, and J. A. Woollam, The Journal of Chemical Physics **62**, 1068 (1975).

[27] T. Yokoya, T. Kiss, A. Chainani, S. Shin, M. Nohara, and H. Takagi, Science **294**, 2518 (2001).

[28] A. Gabovich, A. Voitenko, and M. Ausloos, Physics Reports **367**, 583 (2002), ISSN 0370-1573.

[29] T. Kiss, T. Yokoya, A. Chainani, S. Shin, T. Hanaguri, M. Nohara, and H. Takagi, Nature Physics **3**, 720 (2007).

[30] V. Olevano, M. Cazzaniga, M. Ferri, L. Caramella, and G. Onida, Phys. Rev. Lett. **112**, 049701 (Jan 2014).

[31] M. Calandra and F. Mauri, Phys. Rev. Lett. **112**, 049702 (Jan 2014).

[32] A. Steinhoff, M. Rösner, F. Jahnke, T. O. Wehling, and C. Gies, Nano Letters **14**, 3743 (2014).

[33] S. Hellmann, M. Beye, C. Sohrt, T. Rohwer, F. Sorgenfrei, H. Redlin, M. Kalläne, M. Marczynski-Bühlow, F. Hennies, M. Bauer, A. Föhlisch, L. Kipp, W. Wurth, and K. Rossnagel, Phys. Rev. Lett. **105**, 187401 (Oct 2010).

[34] J. C. Petersen, S. Kaiser, N. Dean, A. Simoncig, H. Y. Liu, A. L. Cavalieri, C. Cacho, I. C. E. Turcu, E. Springate, F. Frassetto, L. Poletto, S. S. Dhesi, H. Berger, and A. Cavalleri, Phys. Rev. Lett. **107**, 177402 (Oct 2011).

[35] The DFT calculations are performed within the LDA using norm-conserving pseudopotentials. For the electronic calculations a $32 \times 32 \times 1$ k-mesh is used ($64 \times 64 \times 1$ for the calculation of $N(\epsilon_F)$), in combination with a Methfessel-Paxton smearing (0.0075 Ry). The lattice parameter is chosen to be 3.122 Å and adjacent layers are separated by ≈ 13 Å. The geometry (S positions) of the simple unit cell is optimized for each electron doping. Phonon band structures and electron-phonon couplings are calculated within the density functional perturbation theory based on the evaluation of the dynamical matrices on a $8 \times 8 \times 1$ q-mesh.

[36] The relaxed structures and the total energies of 1×1 and 2×1 supercells for several doping concentrations are calculated within the LDA. Both calculations are performed on $32 \times 32 \times 1$ k-meshes ($16 \times 32 \times 1$ in the latter case). The tetrathedron method is applied to obtain accurate total energies.

[37] For these calculations the PAW method in the LDA as implemented in VASP has been used.